Journal of Alloys and Compounds 509 (2011) 2186–2191

Contents lists available at ScienceDirect

Journal of Alloys and Compounds

journal homepage: www.elsevier.com/locate/jallcom

Zn_2SnO_4–SnO_2 heterojunction nanocomposites for dye-sensitized solar cells

Bihui Li[a], Lijuan Luo[a], Ting Xiao[a], Xiaoyan Hu[a], Lu Lu[b], Jianbo Wang[b], Yiwen Tang[a,*]

[a] Institute of Nano-science and Technology, Central China Normal University, Wuhan, 430079, China
[b] Department of Physics, Wuhan University, Wuhan 430072, China

ARTICLE INFO

Article history:
Received 18 July 2010
Received in revised form 26 October 2010
Accepted 28 October 2010
Available online 12 November 2010

Keywords:
Heterojunction
Zn_2SnO_4
SnO_2
DSSCs

ABSTRACT

Zn_2SnO_4–SnO_2 heterojunction nanocomposites (ZTO–SnO_2) with high mass amount of ZTO were synthesized by a two-step technique. The route involves firstly the synthesis of monodispersed $ZnSn(OH)_6$ nanocubes with a 50–60 nm edge length as precursors by simple coprecipitation of $Na_2SnO_3{\cdot}3H_2O$ and $ZnCl_2$ aqueous solution, assisted by ultrasonic treatment and then followed by calcination of the precursors at 800 °C under N_2 atmosphere. The as-synthesized nanoparticles were characterized by X-ray diffractometer (XRD), scanning electron microscopy (SEM) and transmission electron microscopy (TEM). Heterojunction between ZTO and SnO_2 nanoparticle was confirmed by the electron energy loss spectroscopy (EELS) elemental mapping and high-resolution TEM (HRTEM). The photovoltaic performance of the ZTO–SnO_2 based DSSC was examined by measuring the *J*-V curves both in dark and under illumination. The results show that the ZTO–SnO_2 based DSSC exhibits superior photovoltaic performance as compared to the single phase ZTO based DSSCs. Under illumination of AM 1.5 simulated sunlight (100 mW/cm^2), the open circuit voltage of the cell based on ZTO–SnO_2 is 706 mV, the short-current density is 2.85 mA/cm^2, and the efficiency is 1.29% which is increased by 43% from 0.90% to 1.29% compared with pure ZTO. The formation of the heterojunctions between ZTO and SnO_2 nanoparticles is believed to reduce the recombination between injected electrons and redox I^-/I_3^- and improve the performance of the DSSC.

1. Introduction

Dye-sensitized solar cell (DSSC) has been regarded as one of most promising photovoltaic device to achieve moderate efficiency at ultra-low cost [1]. The DSSCs are typically constructed from thick films of binary oxides semiconductor nanoparticles that are sintered into mesoporous network with a large internal surface area for the adsorption of light harvesting dye molecules, such as TiO_2 [1], SnO_2 [2], and ZnO [3] films. Recently, people are pursuing some new materials for replacing the widely used TiO_2 in order to avoid its limitations [4]. Titanate [5,6] and stannate [7,8] are the only two kinds of ternary oxides reported for DSSCs support. Both Lana-Villareal and Wu agree in that Zn_2SnO_4 (ZTO) is a promising material for DSSCs although the efficiency (3.8%) of its corresponding DSSC is not high enough. The ternary oxide is more attractive than its simple binary components (ZnO and SnO_2) as the electrode material for DSSCs because it has been demonstrated that ZTO-based cells have also overcome the stability problem associated with against acidic dyes [7].

In DSSCs, the recombination of the photo-excited electrons with the electrolyte ions is one of the principal factors that limits the photocurrent quantum efficiency and to some extent the V_{oc} [9]. For suppressing the recombination, the major strategy is coating a thin layer of insulating oxide (e.g. Al_2O_3 [10], MgO [11], SiO_2 [12], ZrO_2 [13], Nb_2O_5 [14], etc.) on the porous semiconductor nanoparticles film. The formation of the energy barrier was found on the semiconductor electrodes, and the suppression of charge recombination has been known due to the tunneling effect that allows electron injection across the barrier (thin insulating oxide layer) and prevents the electron leakage from the semiconductor to the electrolyte ions. Another strategy is the formation of heterojunction between two oxides. By coupling different semiconductor oxides, more efficient spatial separation of photogenerated charges (D^+ and e^-) resulting from the marching relative energy band positions of these two semiconductors occurs and suppresses recombination [9]. So far, variety of coupled semiconductor system, including ZnO–SnO_2 [15], ZnO–SiO_2 [16], TiO_2–Al_2O_3 [17], have been studied.

ZTO and SnO_2 nanocrystals are both DSSCs materials, with direct band gaps of about 3.6 eV [18,19]. When ZTO is coupled with SnO_2 and being used as photoanode in DSSC, SnO_2 could act as a sink for the photogenerated electrons because the conduction band (CB) position of ZTO is higher than that of SnO_2. This charge transfer will increase the spatial separation of injected electrons and oxidized

* Corresponding author. Tel.: +86 27 67867947; fax: +86 27 67861185.
E-mail address: ywtang@phy.ccnu.edu.cn (Y. Tang).

0925-8388/$ – see front matter © 2010 Elsevier B.V. All rights reserved.
doi:10.1016/j.jallcom.2010.10.184

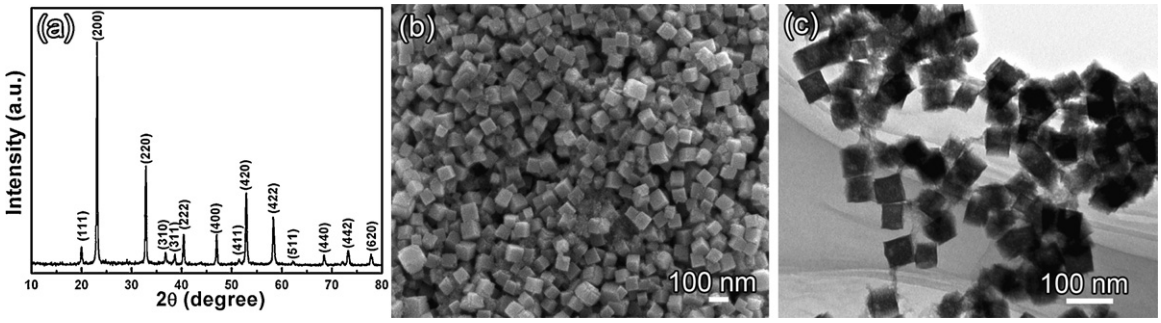

Fig. 1. XRD pattern (a), SEM image (b) and TEM image (c) of the $ZnSn(OH)_6$ precursors.

dyes/redox couple, and thus enhance the efficiency of the corresponding DSSCs. In the present study, ZTO–SnO_2 heterojunction nanocomposites with high mass amount of ZTO are successfully obtained via a two-step route, and their photovoltaic performances in DSSCs are studied. The route involves first the synthesis of monodispersed $ZnSn(OH)_6$ nanocubes as precursors by simple coprecipitation of $Na_2SnO_3{\cdot}3H_2O$ and $ZnCl_2$ aqueous solution, assisted by ultrasonic treatment and then followed by calcination of the precursors at 800 °C under N_2 atmosphere. We present DSSCs based on ZTO–SnO_2 sensitized with $(TBA)_2$cis-Ru(Hdcbpy)$_2$(NCS) (called N719) as working electrodes. The measurement indicates that the photovoltaic performance of the ZTO–SnO_2 electrode was superior to pure ZTO, pure SnO_2 and Pm-ZTO–SnO_2 (physical mixture of ZTO and SnO_2 nanoparticles having the same ZTO/SnO_2 composition) electrodes. The result can be explained by the formation of the heterojunctions between ZTO and SnO_2 nanoparticles.

2. Experimental

2.1. Preparation of ZTO–SnO_2 heterojunctions

Sodium stannate ($Na_2SnO_3{\cdot}3H_2O$) and zinc chloride ($ZnCl_2$) were of analytical grade and used as supplied. $Na_2SnO_3{\cdot}3H_2O$ was dissolved in distilled water, and added dropwise into 100 mL solution of $ZnCl_2$ (0.05 mol/L) with ultrasonically treated for 10 min. The resultant $ZnSn(OH)_6$ was filtered, washed with distilled water and ethanol, and then dried. Subsequently, the $ZnSn(OH)_6$ precursors were calcined at 800 °C for 5 h in N_2 atmosphere.

For the purpose of comparison, pure SnO_2 and pure ZTO nanoparticles were also prepared. ZTO colloid was synthesized according to the hydrothermal method reported in the literature [7]. Tert-butylamine aqueous solution was added dropwise to the mixed solution (water/ethylene glycol, v/v = 1:1) of $ZnCl_2$ and tin chloride pentahydrate ($SnCl_4{\cdot}5H_2O$), then the slurry was transferred to autoclave and kept at 175 °C for 12 h. SnO_2 nanoparticles were obtained by hydrothermal treatment the slurry after adding NaOH solution into $SnCl_4$ at 160 °C for 24 h. Additionally, the composite without heterojunction between SnO_2 and ZTO nanoparticles was prepared by a physical mixing method. In this method, pure SnO_2 and pure ZTO powders were weighed according to ZTO:SnO_2 = 67:33 and subsequently physically mixed in a ball miller with a rotating rate of 450 rpm for 4 h.

2.2. Samples characterization

X-ray diffraction (XRD) patterns were obtained for the samples by using DX-2500 X-ray diffractometer (Dandong, China) with monochromatized Cu Kα radiation (λ = 1.5418 Å). The morphology and structure of the as-synthesized product were characterized using a JEOL JSM-6700F scanning electron microscope (SEM), transmission electron microscopy, selected area electron diffraction and high-resolution TEM (TEM/HRTEM/SAED, JEOL JEM-2010(HT) & JEM-2010FEF). The specific surface area of the final product was determined by using Belsorp-mini II instrument (Ankersmid Co. Ltd.) in the method of Brunauer–Emmett–Teller (BET) nitrogen adsorption and desorption. Optical absorptions of the product were studied by employing Perkin–Elmer Lambda 35 UV–vis spectrophotometer.

2.3. DSSCs preparation

A colloidal mixture was prepared by grinding together 1 g as-synthesized product, 5 mL ethanol, 0.5 mL acetylacetone and 0.2 mL Triton X-100 in a mortar for 1 h. The colloid was dropped on the transparent conductive glasses (SnO_2: F, FTO) with compact TiO_2 nanoparticles about 10 nm and spread uniformly by a glass rod. Then the films were fired at 500 °C for 60 min in atmosphere. Thick films were obtained after repeating above procedure several times. The counter electrode was FTO glass on which Pt was deposited by sputtering. The electrolyte was an acetonitrile/valeronitrile (85:15) based solution containing 0.03 M iodine, 0.6 M 1-butyl-3-methylimidazolium iodide (BMII), 0.1 M guanidinium thiocyanate and 0.5 M 4-tert-butylpyridine. The N719-coated film was illuminated through the conducting glass support with an Oriel 69920 solar simulator as light source. Series of *J–V* curves were monitored and recorded using a Princeton Research Model 263A Potentiostat/Galvanostat. The typical active electrode area was 0.08 cm^2.

3. Results and discussion

Fig. 1a shows the XRD pattern of the precursor. All the diffraction peaks can be indexed to a pure cubic $ZnSn(OH)_6$ structure (JCPDS, No. 73-2384) with a lattice parameter of 7.80 Å. All the peaks are sharp suggesting the high crystallinity of the as-synthesized product. The SEM and TEM images in Fig. 1b and c indicate that the as-synthesized $ZnSn(OH)_6$ is a cubic structure and the sizes are almost monodisperse. All of the nanocubes seem to be mutually separated without agglomeration. The average cubic edge length is in the range of 50–60 nm. The $ZnSn(OH)_6$ nanoparticles show cubic shape mainly because of their intrinsic structures having cubic symmetry. In preparing $ZnSn(OH)_6$, it was noted that the ultrasonic treatment is crucial to form uniform cubes. Only big aggregates composed of $ZnSn(OH)_6$ nanoparticles were obtained by vigorous stirring the reactant solution but without ultrasound irradiation. It is well known that ultrasonic cavitation in liquid may release enormous energy and improve the ion-diffusion rate which is effective for deagglomeration [20]. The synthesis procedure was occurred in room temperature and without any surfactant. Compared to the hydrothermal method by using PVP as surfactant to fabricate the $ZnSn(OH)_6$ nanocubes [21], our method is facile and low-cost.

In order to obtain ZTO–SnO_2 composites from the $ZnSn(OH)_6$ precursors, thermal behavior of the precursors was examined by thermo gravimetric (TG) and differential thermal analysis (DTA). As observed, a sharp endothermic peak in the DTA curve (in Fig. 2)

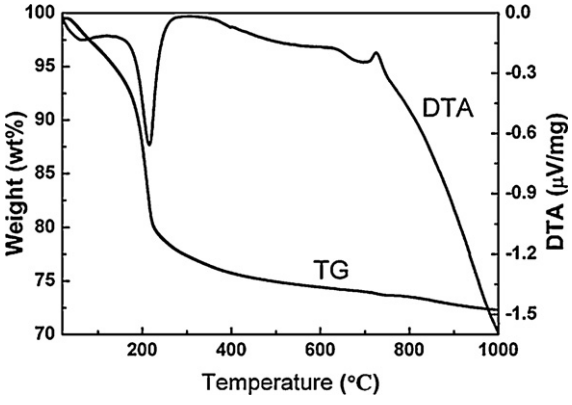

Fig. 2. TG and DTA curves of $ZnSn(OH)_6$ precursors.

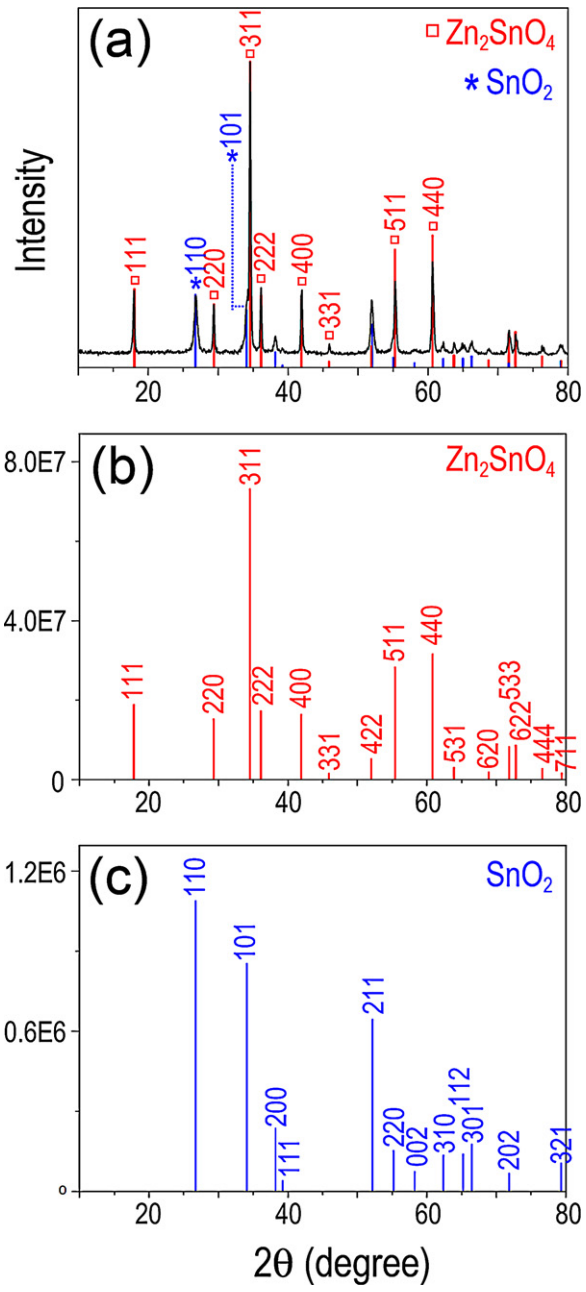

Fig. 3. (a) XRD pattern of the calcined products. (b and c) Calculated XRD patterns of Zn_2SnO_4 and SnO_2.

at 215.6 °C corresponds to a continuous mass loss of 21.2% from 80 °C to 368 °C in the TG curve, which could be attributed to the loss of the three water molecules according to the equation:

$$ZnSn(OH)_6 \rightarrow ZnSnO_3 + 3H_2O$$

But its total mass loss is higher than the theoretical value (18.9%) calculated from the above equation. This difference may be attributed to the release of absorbed water in the air. An exothermic peak at 724.5 °C can be observed, which is attributed to the change in phase from the amorphous to crystalline state and the decomposition of $ZnSnO_3$ according to the following equation:

$$2ZnSnO_3 \rightarrow Zn_2SnO_4 + SnO_2$$

On the basis of the thermal measurement result, we thermally treated $ZnSn(OH)_6$ at 800 °C for 5 h. The XRD pattern of the final samples is shown in Fig. 3a. No extra reflections are observed except for those of ZTO (JCPDS, No. 73-1725) and SnO_2 (JCPDS, No. 77-0451). This makes it possible for quantitative determination of phase composition by applying the 'adiabatic principle' [22]. The mass fractions estimated from integrated intensities of $\{1\,1\,1\}_{ZTO}$ and $\{1\,1\,0\}_{SnO_2}$ are $W_{ZTO} \approx 67.07\%$ and $W_{SnO_2} \approx 32.93\%$, respectively. Additionally, their estimated average sizes of the nanoparticles are 60–70 nm (ZTO) and 20–30 nm (SnO_2), respectively. Fig. 3b and c are calculated XRD patterns of ZTO and SnO_2, whose intensities are not normalized. The composite pattern based on estimated mass fractions is superimposed on the experimental data in Fig. 3a, which shows good coincidence.

The morphology of the final ZTO–SnO_2 composites after thermal treatment is shown in Fig. 4. The SEM and TEM images in Fig. 4 indicate that the appearance of the product is not only multifaceted particles but also have smaller spherical particles. The surface of the multifaceted particles is covered with the spherical nanoparticles. The inserted selected area electron diffraction pattern (SAED) in Fig. 4b confirms the crystalline nature of the nanoparticles and the composites to be a mixture of the cubic ZTO (a) and the tetragonal-phase SnO_2 (b), which is consistent with the observation from XRD patterns (Fig. 3a). A typical TEM image of the composite and the corresponding X-ray elemental maps shown in Fig. 5 give an intuitionistic image for demonstrating the smaller spherical particles being SnO_2 and the multifaceted particles being ZTO. A HRTEM image of the ZTO–SnO_2 interface in Fig. 5d shows that a kind of composite heterojunction forms between ZTO and SnO_2 particles. The fringe spacing of 3.36 Å can be indexed to the (0 0 1) plane of SnO_2 and that of 3.02 Å can be attributed to the (2 2 0) plane of ZTO. Dislocations were observed at the ZTO–SnO_2 interface to relax the misfit stress of two phases and reduce the interfacial elastic energy. The dislocation formation was widely reported for crystal growth in lattice-mismatched system [23] and alloy evolution under thermal exposure [24].

The BET surface area of ZTO–SnO_2 composites is 13.6 $m^2\,g^{-1}$ which is not a quite high value. However, it is still larger than that of ZTO–SnO_2 composite reported by Moon et al. [25], in which the highest BET surface is 4.3 $m^2\,g^{-1}$ in different ration of the product. The enlarged BET is attributed to the much smaller particle sizes of ZTO and SnO_2 than that reported in Ref. [25].

UV–vis absorbance spectrum of the ZTO–SnO_2 composites is shown in Fig. 6 and the spectra of pure ZTO, SnO_2 and Pm-ZTO–SnO_2 are presented also. The band gaps of ZTO–SnO_2, ZTO, SnO_2 and Pm-ZTO–SnO_2 were estimated at 3.63 eV, 3.69 eV, 3.61 eV and 3.68 eV. The band gap of energy of ZTO–SnO_2 is lower than that of pure ZTO. It may be attributed to the synergistic effect by the heterojunction between ZTO and SnO_2 nanoparticles. The similar phenomenon in ZnO–SnO_2 coupled catalysts is reported by Lim and co-workers [15].

The photovoltaic performance of ZTO–SnO_2 in DSSC is examined together with the cells based on pure ZTO, SnO_2 and Pm-ZTO–SnO_2 electrode of comparable thickness (about 8 μm) by measuring the photocurrent density–voltage (J–V) curves both in dark and under illumination. The morphology of the pure ZTO and pure SnO_2 nanoparticles are almost similar as that in Fig. 4a, respectively. Fig. 7 presents the J–V curves of DSSC based on these electrodes and N719 as a dye sensitizer. The corresponding solar cell parameters are summarized in Table 1. As observed in Table 1, ZTO–SnO_2 based DSSC exhibits the superior photovoltaic performance compared to the pure ZTO or SnO_2 electrode, the J_{sc}, V_{oc} and η is 2.85 mA/cm^2, 706 mV and 1.29% under simulated illumination with a light intensity of 100 mW/cm^2.

In the present experiment, the V_{oc} of the cell based on pure ZTO is 674 mV, which is higher than the value of TiO_2 (not shown here). This result is corresponding to the report by Lana-Villarreal et al. [8] who considered the position of the conduction band (CB) for ZTO is located at higher energy than for TiO_2. The CB of SnO_2 is 0.45 V lower

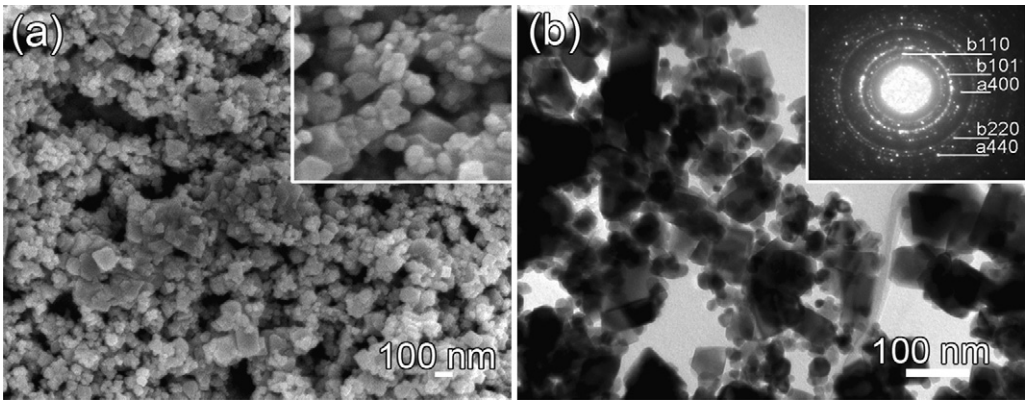

Fig. 4. SEM (a) and TEM (b) image of ZTO–SnO_2.

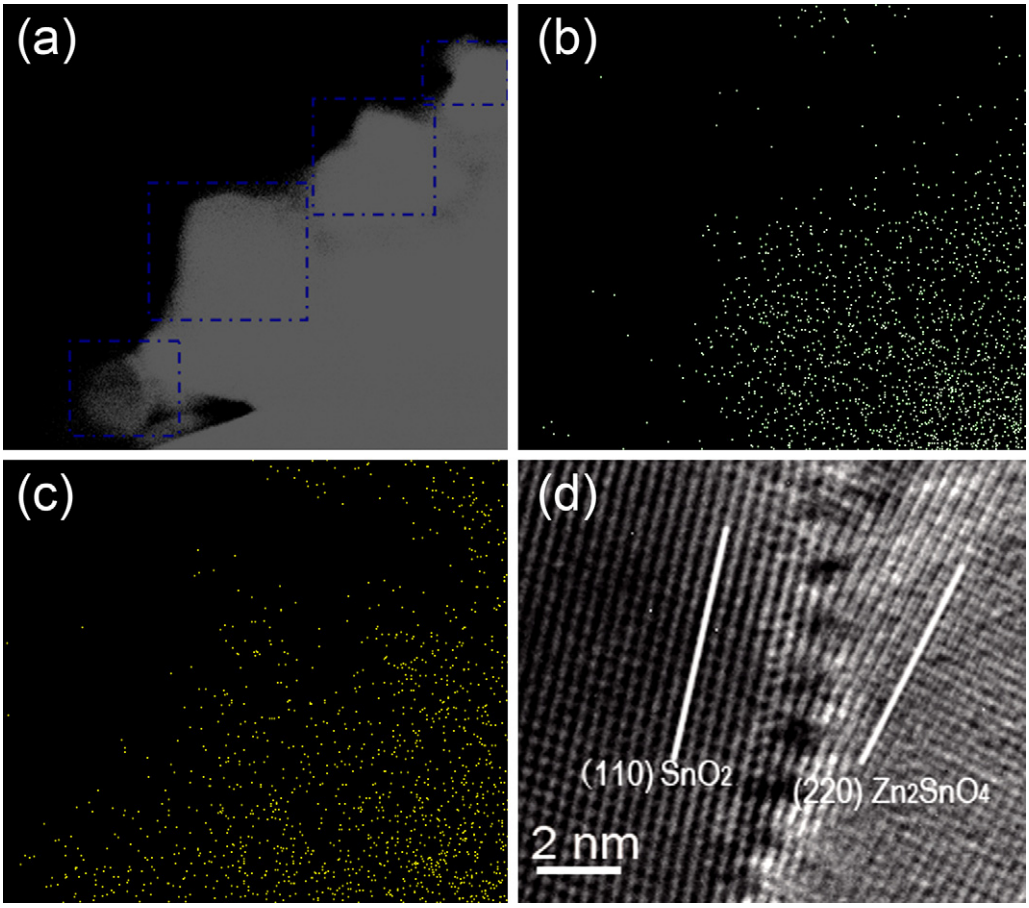

Fig. 5. (a–c) EELS elemental mapping results, corresponding to Zn (b), Sn (c), respectively, (d) HRTEM of the interface between ZTO and SnO_2 particles.

Table 1
Current–voltage characteristics of DSSCs based on different photoanode and the specific surface area of photoanode materials.

Electrode	J_{sc} (mA/cm^2)	V_{oc} (mV)	FF	η (%)	Specific surface area (m^2/g)
ZTO	1.99	674	0.67	0.90	50.9
ZTO–SnO_2	2.85	706	0.63	1.29	13.6.
Pm-ZTO–SnO_2	1.29	555	0.56	0.39	103.0
SnO_2	5.66	149	0.34	0.28	158.4

than that of TiO_2 [19] so it can be proposed that the CB edge potential of ZTO is more negative than that of SnO_2. The energy band structure diagram in the ZTO–SnO_2 heterojunction is elucidated schematically in Fig. 8. Under illumination of AM 1.5 simulated sunlight, an excited dye molecule on a ZTO particle could inject an electron to the CB of ZTO which is interlinked with SnO_2 particles. The injected electron is not enriched on the FTO back contact or recombines as usual, while the electron easily transfers to the CB of the SnO_2 which is lower than ZTO via interfaces. It is favourable for the separation of negative and positive charges and it reduces the probability of the injected electron recombination with the redox I^-/I_3^- or the oxide dye. As a result, the injected electrons can accumulate effectively in the FTO back contact which could also increase

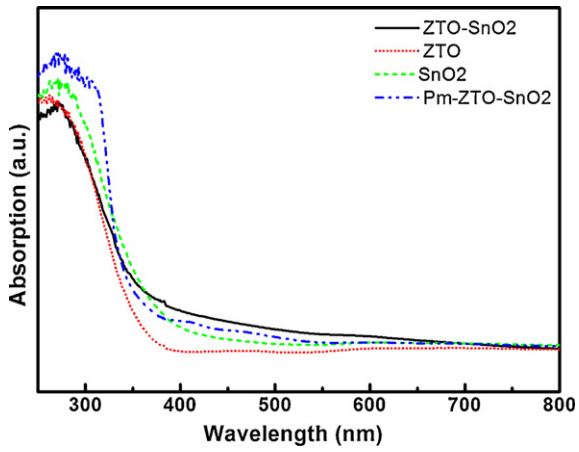

Fig. 6. UV–vis absorption spectrums of ZTO, ZTO–SnO_2, Pm-ZTO–SnO_2 and SnO_2.

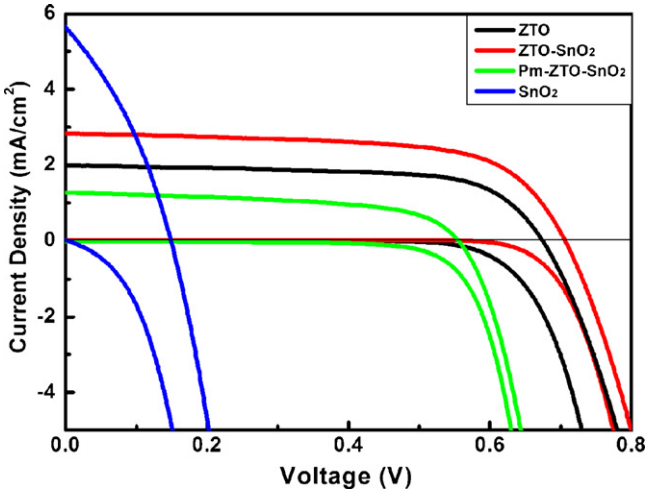

Fig. 7. *J–V* curves of DSSCs based on ZTO, ZTO–SnO_2, Pm-ZTO–SnO_2 and SnO_2.

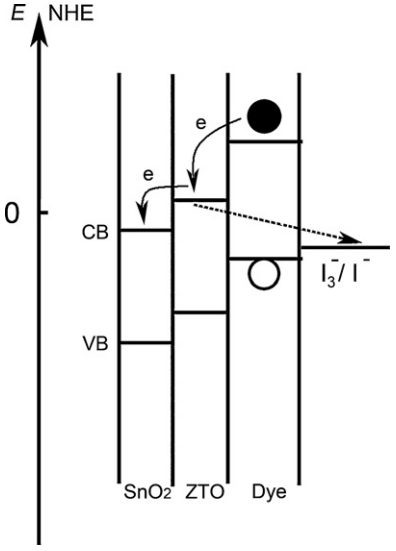

Fig. 8. The energy level diagram in ZTO–SnO_2 heterojunction.

V_{oc} [26]. The recombination between the injected electrons on the CB of the photoanode material and the I^-/I_3^- is well known to be the main pathway for charge recombination in DSSC systems [27]. However, V_{oc} may be also influenced by SnO_2 for its lower conduction band positions comparing with ZTO. But the suppression of recombination to increase V_{oc} occupies the leading role which caused the ZTO–SnO_2 based cell exhibits larger V_{oc} than the pure ZTO based DSSC.

Although the band potentials of two semiconductors (ZTO and SnO_2) can fulfill the thermodynamics conditions for the interparticle charge transfer, the presence of the heterojunction is additionally needed to allow the highly efficient interparticle charge transfer. The composite prepared by the two-step method possesses heterojunction caused by ionic thermal diffusion. In order to elucidate the significance of heterojunction, we further prepared 67/33 ZTO/SnO_2 combined semiconductors Pm-ZTO–SnO_2, without heterojunction, by a physical mixing method as a reference. Pure SnO_2 and pure ZTO powders physically mixed in a ball miller with a rotating rate of 450 rpm for 4 h. The wide and weak diffraction peaks (not shown here) of the XRD pattern of SnO_2 suggest its poor crystallinity. And the SnO_2 mixed with ZTO by grinding would obtain worse crystalline for Pm-ZTO–SnO_2. A large number of defects and the poor crystallinity resulting from the grinding may facilitate the injected electron recombination in the Pm-ZTO–SnO_2 based DSSC. As seen in Fig. 7 and Table 1, the Pm-ZTO–SnO_2 based DSSC shows a rather low photovoltaic performance as compared to the ZTO–SnO_2. This implies the superiority of the two-step method. The main advantage of the method is the formation of heterojunctions between the two materials, making the charge transportations via interfaces and giving rise to the decrease of charge recombination. It is also interesting that the V_{oc} of Pm-ZTO–SnO_2 based DSSC is even lower than that of ZTO based cells. It may be due to the low V_{oc} of the pure SnO_2 based DSSC which is dragged the whole performance down in Pm-ZTO–SnO_2 based DSSC. Furthermore, the large aggregates formed by SnO_2 particles also block the transport of electrons [28].

In order to testify the suppressing recombination in ZTO–SnO_2 based cell, the BET surface area of the four kinds of photoanodes which would affect the J_{sc} is investigated and summarized in Table 1. The calculated BET surface area of pure ZTO, SnO_2 and Pm-ZTO–SnO_2 is 50.9, 158.4 and 103.0 $m^2\,g^{-1}$, respectively, while the BET surface area of ZTO–SnO_2 is 13.6 $m^2\,g^{-1}$. Given that the surface areas of ZTO, SnO_2 and Pm-ZTO–SnO_2 are much greater than that of ZTO–SnO_2, one would expect ZTO, SnO_2 or Pm-ZTO–SnO_2 based DSSCs to show substantially higher J_{sc} than the ZTO–SnO_2 based DSSCs due to the more adsorption of dye. However, the result is contrary to the assumption except SnO_2. A small amount of dye adsorption but a high J_{sc} is in ZTO–SnO_2 based cell, which indicates that the improvement on J_{sc} is mainly caused by suppressing recombination in the ZTO–SnO_2 based DSSC.

To clarify the effect of the charge recombination in this system, the current–voltage characteristic of the films under dark conditions were measured as shown in Fig. 7. The onset of the dark current for DSSC based on pure SnO_2, pure ZTO and Pm-ZTO–SnO_2 is obviously more negative than that for ZTO–SnO_2 based DSSC indicating that charge recombination between injected electrons and I_3^- being retarded in the heterojunctions photoanode. The reduction of dark current in ZTO–SnO_2 heterojunction accounts for the increased V_{oc} in the system.

4. Conclusions

In this work, ZTO–SnO_2 heterojunction composites were synthesized from nearly monodisperse $ZnSn(OH)_6$ nanocubes as precursors. It is beneficial to prepare precursors without using any surfactant but by assisting ultrasonic treatment. The EELS and HRTEM investigations indicated that the heterojunctions were formed in the composites between ZTO and SnO_2 nanoparticles after thermal treatment of $ZnSn(OH)_6$ nanocubes. The ZTO–SnO_2 based DSSC shows superior photovoltaic performance than single

phase ZTO or Pm-ZTO–SnO_2 based DSSC. The obvious improvement in the photovoltaic performance as ZTO is combined over SnO_2 is mainly ascribed to the efficient injected electrons transfer between the two materials via heterojunctions and consequent suppress the recommbination between injected electrons and redox I^-/I_3^-.

Acknowledgement

Financial supported by self-determined research funds of CCNU from the colleges' basic research and operation of MOE of China (CCNU09A02011, 2009034).

References

[1] B. O'Regan, M. Grätzel, Nature 353 (1991) 737–739.
[2] Y. Fukai, Y. Kondo, S. Mori, E. Suzuki, Electrochem. Commun. 9 (2007) 1439–1443.
[3] Z.G. Chen, Y.W. Tang, L.S. Zhang, L.J. Luo, Electrochim. Acta 51 (2006) 5870–5875.
[4] L. Grinis, S. Kotlyar, S. Rühle, J. Grinblat, A. Zaban, Adv. Funct. Mater. 20 (2010) 282–288.
[5] S. Burnside, J.-E. Moser, K. Brooks, M. Grätzel, J. Phys. Chem. B 103 (1999) 9328–9332.
[6] Y. Li, X.P. Gao, G.R. Li, G.L. Pan, T.Y. Yan, H.Y. Zhu, J. Phys. Chem. C 113 (2009) 4386–4394.
[7] B. Tan, E. Toman, Y.G. Li, Y.Y. W., J. Am. Chem. Soc. 129 (2007) 4162–4163.
[8] T. Lana-Villarreal, G. Boschloo, A. Hagfeldt, J. Phys. Chem. C 111 (2007) 5549–5556.
[9] K. Tennakone, G.R.R.A. Kumara, I.R.M. Kottegoda, V.P.S. Perera, Chem. Commun. (1999) 15–16.
[10] B.C. O'Regan, S. Scully, A.C. Mayer, J. Phys. Chem. B 109 (2005) 4616–4623.
[11] T. Taguchi, X.T. Zhang, I. Sutanto, K. Tokuhiro, T.N. Rao, H. Watanabe, T. Nakamori, M. Uragami, A. Fujishima, Chem. Commun. (2003) 2480–2481.
[12] T.-V. Nguyen, H.-C. Lee, M.A. Khan, O.-B. Yang, Sol. Energy 81 (2007) 529–534.
[13] Y. Diamant, S. Chappel, S.G. Chen, O. Melamed, A. Zaban, Coord. Chem. Rev. 248 (2004) 1271–1276.
[14] S.G. Chen, S. Chappel, Y. Diamant, A. Zaban, Chem. Mater. 13 (2001) 4629–4634.
[15] H.H. Wang, S. Baek, J. Lee, S. Lim, Chem. Eng. J. 146 (2009) 355–361.
[16] H. Wang, X.H. Zhang, X. Fan, C.-S. Lee, S.-T. Lee, Chem. Commun. (2009) 5916–5918.
[17] W. Lin, L. Lin, Y.X. Zhu, Y.C. Xie, K. Scheurell, E. Kemnitz, Chin. J. Chem. 23 (2005) 1333–1338.
[18] T.J. Coutts, D.L. Young, X. Li, W.P. Mulligan, X. Wu, J. Vac. Sci. Technol. A 18 (2000) 2646–2660.
[19] I. Bedjia, S. Hotchandani, P.V. Kamat, J. Phys. Chem. 98 (1994) 4133–4140.
[20] K.S. Suslick, S.B. Choe, A.A. Cichowlas, M.W. Grinstaff, Nature 353 (1991) 414–416.
[21] Z. Lu, Y. Tang, Mater. Chem. Phys. 92 (2005) 5–9.
[22] F. Chung, J. Appl. Crystallogr. 8 (1975) 17–19.
[23] B. Nikoobakht, S. Eustis, A. Herzing, J. Phys. Chem. C 113 (2009) 7031–7037.
[24] L.R. Liu, T. Jin, N.R. Zhao, Z.H. Wang, X.F. Sun, H.R. Guan, Z.Q. Hu, Mater. Lett. 57 (2003) 4540–4546.
[25] W.J. Moon, J.H. Yu, G.M. Choi, Sens. Actuators B 80 (2001) 21–27.
[26] J.E. Kroeze, N. Hirata, S. Koops, Md.K. Nazeeruddin, L. Schmidt-Mende, M. Grätzel, J.R. Durrant, J. Am. Chem. Soc. 128 (2006) 16376–16383.
[27] G. Schlichthörl, S.Y. Huang, J. Sprague, A.J. Frank, J. Phys. Chem. B 101 (1997) 8141–8155.
[28] S. Ito, Y. Makari, T. Kitamura, Y. Wada, S. Yanagida, J. Mater. Chem. 14 (2004) 385–390.